Direct Numerical Simulation of Shockwave and Turbulent Boundary Layer Interactions

Stephan Priebe* and M. Pino Martin†

Department of Mechanical and Aerospace Engineering, Princeton University, Princeton, NJ 08544

Past and current work on direct numerical simulations of shockwave and turbulent boundary layer interactions at the CRoCCo Laboratory at Princeton University is presented. Direct numerical simulations of compression ramp and reflected shock configurations are discussed, with particular emphasis on the validation of the simulations against experiments at matching flow conditions. The low-frequency motion of the shock system is analyzed. A 'long-time' DNS of a Mach 3 boundary layer, which will serve as an inflow boundary condition for future STBLI simulations, is presented. In an effort to extend the simulations to higher, hypersonic Mach numbers, the DNS of a Mach 8 boundary layer is also briefly presented.

Nomenclature

δ	99% thickness of the incoming boundary layer
C_f	skin friction coefficient
f	filter function
f_s	shock frequency
i, j, k	computational coordinate in the streamwise, spanwise and wall-normal directions
L_{sep}	length of separated region
M	Mach number
p'	pressure fluctuation
$p_{w,rms}$	r.m.s. of wall-pressure
p_w	mean wall-pressure
Re_θ	Reynolds number based on the momentum thickness, θ
Re_{δ^*}	Reynolds number based on the displacement thickness, δ^*
$S_L = f_s L_{sep}/U_\infty$	shock Strouhal number
T	temperature
U_∞	freestream velocity
ρ	density
x,y,z	streamwise, spanwise and wall-normal coordinate

Subscripts

∞	freestream quantity
w	wall quantity

I. Introduction

It has been observed in many experimental studies of shockwave and turbulent boundary layer interactions[1] (STBLI) that the flow is highly unsteady, particularly when the shockwave is sufficiently strong to cause flow separation. In these 'strong' interactions, the shock system translates back and forth in the streamwise

*Graduate Student, AIAA Student Member.

†Assistant Professor, AIAA Senior Member.

direction with a relatively low frequency, as compared to the characteristic frequency of the turbulent motions in the incoming boundary layer. This shock unsteadiness is of significant practical importance. It leads to large-scale, low-frequency fluctuations of the pressure and heat loading on the wall, which may be detrimental to the structural and thermal integrity of the vehicle.

In addition to the vast body of experimental results, there have recently been a number of Large Eddy Simulations (LESs) and Direct Numerical Simulations (DNSs) of STBLI. Most of these simulations have been concerned with the compression ramp configuration, which is also the most studied experimentally. The inviscid flow scenario for this configuration is shown in figure 1(a). The less studied reflected shock configuration is shown schematically in figure 1(b) for the inviscid case.

We briefly mention several simulations here, a more complete list can be found elsewhere.[2] Garnier et al.[3] performed a LES of a reflected STBLI at Mach 2.3 and Re_{δ^*} 19,132. The flow deflection through the incident shock was 8°. As noted by the authors, the simulation was not run for a long enough time to investigate the low-frequency shock motion. More recently, Touber and Sandham[4] performed a LES of the reflected STBLI at Mach 2.3 and Re_θ 5900, and investigated the low-frequency shock motion. Adams[5] performed the first DNS of a compression corner flow, at M=3 and $Re_\theta = 1685$. Pirozzoli and Grasso[6] carried out a DNS of a reflected STBLI at Mach 2.25 and Re_θ 3725 for a deflection angle through the incident shock of 8.1°. They proposed a mechanism whereby acoustic feedback in the separation bubble drives the shock motion.

The purpose of this paper is to present past and current work on DNS of STBLI at the CRoCCo Laboratory at Princeton University. Particular emphasis is placed on the investigation of the low-frequency shock unsteadiness and possible physical mechanisms that might be driving it. The paper is structured as follows: The DNS data set is introduced in section II, and the validation of the DNS against experiments at matching flow conditions is reviewed. In section III, we discuss the low-frequency shock unsteadiness as observed in the DNS data. Current efforts to compute the DNS for longer times in order to enable further analysis of the physical mechanism that drives the shock motion are discussed. Specifically, a long-time DNS of a Mach 3 boundary layer, which is intended to be used as an inlet boundary condition for future STBLI simulations, is presented in section IV. Efforts towards performing DNS of STBLI at higher, hypersonic Mach numbers, specifically at Mach 8, are also presented in section IV.

II. Accurate simulations

In this section we present the direct numerical simulations. Since many of the results have already been reported elsewhere, the presentation here is a brief review, which emphasizes on the validation of the simulations against experimental results. The purpose of this section is to summarize the results that show the accuracy of the DNS and to set the stage for the discussion of the shock unsteadiness in the next section.

II.A. Numerical method

The viscous fluxes are discretized in space using standard 4th-order accurate central differencing. Time integration is performed with a 3rd-order accurate, low-storage Runge-Kutta algorithm. For the spatial discretization of the inviscid fluxes, we use a modified 4th-order accurate weighted essentially nonoscillatory scheme (WENO).

The original WENO finite-difference scheme was introduced by Jiang and Shu.[7] The basic idea is to determine the numerical flux as a weighted sum of fluxes on candidate stencils. In smooth regions of the flow, optimal weights are used, which are designed to give maximum accuracy in the original scheme. The presence of discontinuities is indicated by a smoothness measurement. Using this smoothness measurement, the fluxes of candidate stencils that contain a discontinuity are given a nearly zero weight. The scheme is said to 'adapt' away from the optimal weights in non-smooth regions of the flow. A detailed description of the original WENO method can be found in the papers by Jiang and Shu,[7] Martin et al.,[8] and Taylor, Wu and Martin ,[9] for example.

As discussed in Wu and Martin,[2] the original WENO scheme is too dissipative for accurate DNS of STBLI. In order to achieve acceptable levels of dissipation, we use a modified WENO method, in which both the linear and the nonlinear part of the scheme have been optimized. Linear optimization refers to the choice of optimal weights which maximizes bandwidth-resolving efficiency and minimizes dissipation in smooth regions of the flow (see Martin et al.[8]). A significant source of numerical dissipation is the nonlinear part of the scheme, that is, the adaptation mechanism that drives the weights away from their optimal values in non-smooth region of the flow. This dissipation can be mitigated by using absolute and relative limiters, which limit the adaptation of WENO.[9,2] In our DNS code, we use both an absolute and a relative limiter, details of which can be found in Wu and Martin.[2]

The flowfield is initialized using the method of Martin.[10] The inflow boundary condition is provided by the rescaling method of Xu and Martin.[11]

II.B. Compression corner

The DNS of the compression corner interaction has been reported by Wu and Martin.[2] Details of the computational setup (domain geometry and size, grid resolution etc.) can be found in their paper. The flow conditions for the DNS are as follows: the incoming boundary layer is at Mach 2.9 and $Re_\theta = 2300$. The ramp angle is 24°.

Figure 2 shows an instantaneous numerical schlieren visualization of the DNS, in which the variable is defined as:

$$NS = c_1 exp[-c_2(x - x_{min})/(x_{max} - x_{min})] \tag{1}$$

where $x = |\nabla\rho|$ and c_1 and c_2 are constants. We use $c_1 = 0.8$ and $c_2 = 10$ in our analysis. This transformation enhances small density gradients in the flow field and resembles experimental schlieren visualizations. All the basic flow features familiar from high Reynolds number experimental visualizations (e.g. Settles, Fitzpatrick and Bogdonoff[12]) are visible. The shock originates upstream of the corner. This is due to the fact that flow is separated in the corner and that the presence of the corner makes itself felt upstream through the subsonic part of the separation bubble. It is also apparent that the shock foot is wrinkled. Several shocklets are seen to originate downstream of the corner and to merge with the main shock.

The DNS code has been validated by Wu and Martin[2] in the context of the compression corner flow against the experiments of Bookey, Wyckham and Smits.[13] The flow conditions for the DNS and experiments match closely.[2,13] Figure 3 shows the mean wall-pressure distribution throughout the interaction for the DNS and the experiments. The error bars for the experiments are at 5%. The agreement is good. In particular, we note that the experimental pressure distribution shows a 'plateau', which is indicative of separated flow. The simulation captures this plateau well, both in terms of its streamwise extent and the pressure level. The DNS also shows good agreement with the experiments for the mean velocity distribution upstream and downstream of the interaction, and for the separation length.[2]

More recently, Ringuette, Wu and Martin[14] validated the fluctuating wall-pressure in the DNS against the experiments by Ringuette and Smits.[15] The flow conditions for the DNS and experiments match closely. Figure 4 plots the normalized r.m.s. of the wall-pressure, $p_{w,rms}/p_w$, versus streamwise distance. Whereas the shape of the curves agrees well, the fluctuation level is generally higher in the DNS than the experiments. In particular, the value of $p_{w,rms}/p_w$ is 2% higher for the DNS in the incoming boundary layer; in the downstream flow, the DNS shows a 4% higher value (as indicated on the figure). Although the magnitudes of the peaks differ, their streamwise location agrees closely. The significant difference in the wall-pressure fluctuation level between the DNS and the experiment may be explained following Ringuette et al.[14] The DNS has a higher level of fluctuations in the freestream. By viewing these fluctuations as uncorrelated noise (this is a valid assumption since the high level of freestream fluctuations is attributable to the uncorrelated fluctuations introduced when initializing the DNS flowfield), one can argue that the wall-pressure fluctuations in the DNS are the sum of the true value, p'_w, and noise, p'_n. It follows immediately that the m.s. of the total DNS wall-pressure signal is $\overline{(p'_w + p'_n)^2} \approx \overline{(p'_w)^2} + \overline{(p'_n)^2}$. Assuming that the noise, p'_n, is equal to the pressure fluctuation in the freestream, an estimate for the amplification of p'_n across the shock is obtained. Using this analysis, it can be shown that the normalized r.m.s. of the noise, $\sqrt{\overline{(p'_n)^2}}/p_w$, is amplified by a factor of approximately 2 across the shock. This agrees with figure 4, which shows that the difference between the DNS and experimental results increases by a factor of 2 across the interaction, namely from approximately 2% upstream of the interaction to 4% downstream.

II.C. Reflected shock configuration

Since our DNS code is general and shock-location-independent, its validation for the compression corner flow means that it can be employed to simulate other STBLI flows with confidence. In this section, we briefly present the DNS of the reflected shock flow. The incoming boundary layer is the same as in the compression corner case above, i.e. the freestream conditions are Mach 2.9 and $Re_\theta = 2300$. The flow deflection through the incident shock is 12°, thus giving a similar pressure rise through the interaction as that produced by the 24° compression ramp. The computational domain and a sample grid are shown in figure 5. In addition to being clustered near the wall, the grid is also clustered in the streamwise direction near the interaction region to ensure sufficient resolution there. The actual grid has $1100\times160\times132$ gridpoints in the streamwise, spanwise and wall-normal direction, respectively.

Figure 6 shows an instantaneous numerical schlieren visualization for the DNS (the variable plotted is given by equation 1). The incident shock, which is generated by the boundary condition in the freestream at the inflow station, originates in the top left corner of the domain and progresses diagonally through the domain to the impingement point. The pressure change propagates through the subsonic flow region, and the flow separates further upstream, where the separation shock is generated. The reflected shock foot is strongly wrinkled, and, as in the compression ramp case, a series of shocklets is seen to originate downstream of the interaction and to merge with the main shock.

III. Shock Unsteadiness

III.A. Background

Smits and Dussauge[1] show that the shock motion may be decomposed into two parts, namely a spanwise wrinkling and a streamwise oscillation. The frequency of the spanwise wrinkling is comparable to the characteristic frequency of the turbulent motions in the incoming boundary layer, U_∞/δ, where δ is the 99% thickness of the incoming boundary layer and U_∞ is the freestream velocity. This must be contrasted with the streamwise oscillation which is at a much lower frequency, typically 1-2 orders of magnitude lower than U_∞/δ. It has been observed that the high-frequency spanwise wrinkling is caused by the structures in the incoming boundary layer, see e.g. the experiments by Erengil and Dolling,[16] Wu and Miles,[17] and the compression ramp DNS by Wu and Martin.[18] The cause of the low-frequency shock motion, however, is less clear. Recently, Ganapathisubramani et al.[19] proposed that elongated, low-momentum regions in the incoming boundary layer, so-called 'superstructures', might be driving the low-frequency shock motion. However, it has also been argued that the shock motion is caused by the downstream separated flow rather than the incoming boundary layer. From their DNS of a reflected STBLI, Pirozzoli and Grasso[6] proposed a mechanism whereby acoustic feedback in the separation bubble drives the shock motion. Dussauge et al.[20] argued that large-scale, three-dimensional structures in the separated flow region could be driving the shock motion.

A qualitative impression of the shock motion in the DNS can be gained from numerical schlieren movies. Such a movie is available online for the reflected shock DNS [a]. The movie illustrates the two parts of the shock motion: The shock foot is seen to 'flap' at a high-frequency, seemingly in response to incoming boundary layer structures, whereas further away from the wall, the shock is seen to translate with a low-frequency in the streamwise direction.

Figure 7 plots instantaneous contours of $|\nabla p|$ at two different wall-normal planes for the compression corner DNS. The shock is visible as the dark region, corresponding to the largest gradients. Figure 7 (a) and (b) are taken at z=2δ above the wall, whereas figure 7 (c) and (d) are taken closer to the wall, at z=0.9δ. Figures 7 (a) and (c) show the same time realization, which occurs $50\delta/U_\infty$ before the time realization shown in (b) and (d). In these plots, SK_m indicates the mean shock location (averaged over the span of the domain and over all the time realizations). In contrast, SK_{sm} indicates the instantaneous, spanwise-mean shock location (no time averaging). The two parts of the shock motion, namely the streamwise translation and the spanwise wrinkling, are apparent from these plots. At both wall-normal locations shown, the shock translates in the streamwise direction between the two flow realizations. From the plots, the amplitude of the streamwise shock translation is seen to be at least of order δ. Whereas the shock is uniform in the spanwise direction at z=2δ, it is 'wrinkled' at z=0.9δ. The wavelength of the spanwise wrinkling is seen to be of order δ.

In the following subsection, we present an analysis of the low-frequency shock motion as observed in the DNS. In particular, we derive an estimate for the shock frequency from the wall-pressure signals. This is followed by a discussion of methodologies to investigate the physical mechanism that drives the low-frequency shock motion.

[a] see http://www.princeton.edu/mae/people/faculty/martin/homepage/data-sets/movies/

III.B. The low-frequency shock unsteadiness in DNS data

The compression corner DNS has been run for a total time of $300\delta/U_\infty$. Figure 8(a) plots the wall-pressure signal for the DNS at three different streamwise locations. Of particular interest are the green and blue signals. The green signal is sampled at the mean-flow separation point, and the blue signal is sampled a short distance further downstream. Both signals display a low-frequency oscillation which may be attributed to the motion of the shock over the measurement points. The frequency of the shock motion can be deduced from the signals' energy spectra in figure 8(b). It is apparent that the green and blue signal have significant energy peaks in the frequency range 0.007-$0.013U_\infty/\delta$. A similar analysis has been performed for the reflected shock DNS, which has been run for a total time of $976\delta/U_\infty$. Several wall-pressure signals and their corresponding spectra are shown in figure 9. As for the compression corner DNS, the signal near the mean-flow separation point displays a low-frequency oscillation due to the shock motion. From the energy spectrum in figure 9(b), we estimate the frequency of the shock motion to be in the range 0.002-$0.006U_\infty/\delta$. This frequency is lower, by about a factor of 2, than in the compression ramp DNS.

From a survey of experimental results covering different STBLI configurations and a wide range of Mach and Reynolds numbers, Dussauge et al.[20] find that the low frequency of the shock motion collapses reasonably well under the following scaling:

$$S_L = \frac{f_s L_{sep}}{U_\infty} \tag{2}$$

where f_s is the shock frequency, L_{sep} is the length of the separated region, and U_∞ is the freestream velocity. The range of values found in the survey is $S_L = 0.02 - 0.05$.

Using the frequencies inferred above from the wall-pressure signals, we find that the Strouhal number is $S_L = 0.03 - 0.05$ for the compression ramp case and $S_L = 0.015 - 0.046$ for the reflected shock case. We may thus conclude that our DNS captures the low-frequency motion of the shock and that the frequency agrees with the survey values found by Dussauge et al.[20]

III.C. Continuing analysis of the physical mechanism driving the low-frequency shock unsteadiness

We briefly summarize the key results that were obtained by Wu and Martin[18] for the compression ramp DNS. They observe that there is a significant positive correlation between the spanwise-mean shock location and separation point. Furthermore, the spanwise-mean shock location and separation point are negatively correlated with the spanwise-mean reattachment point. The motion of the separation point (and that of the shock) is seen to lag the reattachment point motion. These observations are consistent with the separation bubble undergoing a contraction/expansion motion, and the shock following this motion with a time lag. Figure 10 plots the mass and area of the reverse flow region. The reverse flow region has been defined as the region where the spanwise-averaged streamwise velocity is negative. It is apparent that the mass and area of the reverse flow region are intermittent and vary at a relatively low frequency. Furthermore, the mass and area track each other closely over time, indicating that the contraction/expansion motion of the separation bubble is not a compressible mode. Wu and Martin[18] also observe the contraction/expansion motion of the separation bubble from DNS data animations. Figure 11 shows six consecutive flow visualizations of the compression ramp DNS, with a timestep of approximately $1\delta/U_\infty$ between the frames. Spanwise-averaged streamlines and contours of pressure gradient are shown. Figures 11 (c)-(f) show how the bubble shrinks rapidly as fluid is ejected at its downstream end. At a later time (which is not shown), the shock moves downstream, following the motion of the separation point.

Similar analyses may be performed for the reflected shock DNS. But, at this stage our ability to gain significant new insights into the physical mechanism of the shock unsteadiness is restricted by the relatively short duration of both DNS datasets. As is apparent from the pressure signals in figures 8(a) and 9(a), the compression ramp DNS contains about three periods of the low-frequency shock motion, and the reflected shock DNS contains about two periods. At least several more periods are required to enable further analysis of the shock unsteadiness. A longer dataset would, for example, enable the analysis of the statistical correlation between the shock motion and the upstream (or downstream) flow, thus shedding further light on whether the shock motion is principally driven by the upstream incoming boundary layer, or by the downstream separated flow. Presently, the cross-correlation spectra are not yet fully converged. A longer dataset would also enable further analysis of the mechanism for the contraction/expansion motion of the separation bubble. The mean streamline bounding the separation bubble in the compression corner case is presently not converged. If enough data were available for it be converged, one could define a control volume that coincides with the mean separation bubble. The fluxes entering and leaving the control volume could be determined. This, or similar, analyses have the potential of clarifying the contraction/expansion cycle of the separation bubble.

The aim must thus be to run the DNS for longer, which presents significant challenges. The reflected shock data presented here, for example, covers a total time of $976\delta/U_\infty$. We have observed that if the DNS is run for much longer to around $1500\delta/U_\infty$, weak normal pressure disturbances appear in the freestream. They are seen to move downstream in the flow direction, and they are periodically re-introduced into the flow by the rescaling method which provides the inflow boundary condition. The disturbances lead to an unacceptable increase of the pressure fluctuations in the freestream, $p_{\infty,rms}$. The level of pressure fluctuations at the wall, $p_{w,rms}$, is also seen to increase. The pressure fluctuations cause an undesired wrinkling of the incident shock. The simulation becomes unphysical and must be stopped.

We note that this problem only occurs for very long run times and does not affect the data shown here. For the reflected shock DNS, the value of $p_{w,rms}/p_w$, remains between 3.5-4.5% for the duration of the DNS data shown here, that is, up to $976\delta/U_\infty$. The same value is found for the compression ramp DNS. This can be seen from figure 4, which shows that $p_{w,rms}/p_w$ is 4% on average for this simulation in the incoming boundary layer. While this is a higher fluctuation level than in the experiments, it is acceptable (see Ringuette et al.[14]). Specifically, the analysis of Ringuette et al.[14] (which has been summarized in section II.B of this paper) shows that by treating the excess fluctuation level in the simulation as uncorrelated noise that does not affect the flow physics, the discrepancy between experiment and DNS downstream of the interaction can be deduced from its value in the undisturbed freestream.

In the next section, we present preliminary results for the DNS of a boundary layer, in which the normal pressure disturbances that appear for very long run times in the original DNS have been eliminated. This DNS data set is intended as an inflow boundary condition for future 'long-time' STBLI simulations.

IV. Other Aspects of the DNS

IV.A. A 'Long-Time' Inflow Boundary Condition

We perform a boundary layer DNS, in which the flowfield is 'filtered' every $75\delta/U_\infty$ according to:

$$u(x,y,z) = \overline{u(z)} + f(z)u'(x,y,z) \tag{3}$$

where u is the filtered variable, $\overline{u}$ is the streamwise-spanwise mean of the unfiltered variable, u' is the fluctuation of the unfiltered variable, and f is the filter function. A value of $f = 0$ means that the fluctuations are completely damped out, whereas $f = 1$ means that the flow is left unchanged. The filter function is defined to depend only on the wall-normal coordinate, z (or, equivalently, the wall-normal computational coordinate, k). It varies according to a hyperbolic tangent function:

$$f(k) = \frac{1}{2}\left\{1 - tanh\left[c\frac{k-k_m}{k_e-k_s}\right]\right\} \tag{4}$$

where k_e and k_s are constants, k_m is defined according to $k_m = (k_e+k_s)/2$, and c is a constant. The constants are chosen such that the filter does not operate on the actual boundary layer and is only 'turned on' in the freestream above z = 1.5δ. This ensures an accurate, physical simulation of the boundary layer while also fulfilling the goal of damping the noise in the freestream. The flow conditions for the DNS presented here are the same as for the STBLI flows presented above. Figure 12 plots the van Driest-transformed velocity profile for the DNS. The profile follows the log law accurately. Figure 13 plots the spanwise-averaged mass-flux signal in the freestream at z = 1.6δ. Both the signal for the original, unfiltered DNS and for the filtered DNS are shown, illustrating that the filtering works to damp the undesired and unphysical growth of the fluctuations in the freestream.

IV.B. Ongoing DNS of STBLI at Mach 8

Ultimately, we would like to run STBLI simulations at higher, hypersonic Mach numbers including chemical reactions. Roe's averaging, which is commonly used to determine the flux Jacobian, is not accurate for reacting flows. We have generalized the flux Jacobian to enable DNS of chemically-reacting, high Mach number, low-density flows. Figure 14 shows an instantaneous numerical schlieren visualization of a Mach 7.8 boundary layer (the variable plotted here is given by equation 1). The Reynolds number based on momentum thickness is $Re_\theta = 5100$. The freestream is at a temperature of $T_\infty = 227.72K$, and the density is $\rho_\infty = 0.0948 kg/m^3$. The ratio of the wall temperature to that in the freestream is $T_w/T_\infty = 11.91$.

V. Conclusions

We have presented and reviewed two DNS data sets, one for compression corner flow and the other for reflected shock flow. The accuracy of the DNS and its validation against experiments at matching conditions has been reviewed. The low-frequency shock unsteadiness is captured in the DNS, and its frequency is shown to agree with the scaling used by Dussauge et al.[20] The physical mechanism of the low-frequency unsteadiness is still unclear. To enable further analysis, several more periods of the unsteadiness are required in the DNS, and efforts in this direction have been presented.

Acknowledgments

This work is supported by the Air Force Office of Scientific Research under grant AF/9550-06-1-0323.

References

[1]Smits, A. J. and Dussauge, J. P., *Turbulent Shear Layers in Supersonic Flow*, Springer Verlag, New York, 2nd ed., 2006.

[2]Wu, M. and Martin, M. P., "Direct Numerical Simulation of Supersonic Turbulent Boundary Layer over a Compression Ramp," *AIAA Journal*, Vol. 45, No. 4, 2007, pp. 879–889.

[3]Garnier, E., Sagaut, P., and Deville, M., "Large Eddy Simulation of Shock/Boundary-Layer Interaction," *AIAA Journal*, Vol. 40, No. 10, 2002, pp. 1935–1944.

[4]Touber, E. and Sandham, N. D., "Oblique Shock Impinging on a Turbulent Boundary Layer: Low-Frequency Mechanisms," *AIAA Paper No. 2008-4170*, June 2008.

[5]Adams, N. A., "Direct Simulation of the Turbulent Boundary Layer Along a Compression Ramp at M=3 and $Re_\theta = 1685$," *J. Fluid Mech.*, Vol. 420, 2000, pp. 47–83.

[6]Pirozzoli, S. and Grasso, F., "Direct Numerical Simulation of Impinging Shock Wave/Turbulent Boundary Layer Interaction at M=2.25," *Physics of Fluids*, Vol. 18, No. 065113, 2006.

[7]Jiang, G. and Shu, C., "Efficient Implementation of Weigted ENO Schemes," *Journal of Computational Physics*, Vol. 126, No. 1, 1996, pp. 202–228.

[8]Martin, M. P., Taylor, E. M., Wu, M., and Weirs, V. G., "A Bandwidth-Optimized WENO Scheme for the Direct Numerical Simulation of Compressible Turbulence," *Journal of Computational Physics*, Vol. 220, 2006, pp. 270–289.

[9]Taylor, E. M., Wu, M., and Martin, M. P., "Optimization of Nonlinear Error Sources for Weighted Essentially Non-oscillatory Methods in Direct Numerical Simulations of Compressible Turbulence," *Journal of Computational Physics*, Vol. 223, 2006, pp. 384–397.

[10]Martin, M. P., "Direct Numerical Simulation of Hypersonic Turbulent Boundary Layers. Part1. Initialization and Comparison with Experiments," *Journal of Fluid Mechanics*, Vol. 570, 2007, pp. 347–364.

[11]Xu, S. and Martin, M. P., "Assessment of Inflow Boundary Conditions for Compressible Boundary Layers," *Physics of Fluids*, Vol. 16, No. 7, 2004, pp. 2623–2639.

[12]Settles, G. S., Fitzpatrick, T., and Bogdonoff, S. M., "Detailed Study of Attached and Separated Compression Corner Flowfields in High Reynolds Number Supersonic Flow," *AIAA Journal*, Vol. 17, No. 6, 1979, pp. 579–585.

[13]Bookey, P. B., Wyckham, C., and Smits, A. J., "Experimental Investigations of Mach 3 Shock-Wave Turbulent Boundary Layer Interactions," *AIAA Paper No. 2005-4899*, June 2005.

[14]Ringuette, M. J., Wu, M., and Martin, M. P., "Low Reynolds Number Effects in a Mach 3 Shock Turbulent Boundary Layer Interaction," *AIAA Journal*, Vol. 46, No. 7, 2008.

[15]Ringuette, M. J. and Smits, A. J., "Wall-Pressure Measurements in a Mach 3 Shock-Wave and Turbulent Boundary Layer Interaction at a DNS-Accessible Reynolds Number," *AIAA Paper No. 2007-4113*, June 2007.

[16]Erengil, M. E. and Dolling, D. S., "Correlation of Separation Shock Motion with Pressure Fluctuations in the Incoming Boundary Layer," *AIAA Journal*, Vol. 29, No. 11, 1991, pp. 1868–1877.

[17]Wu, P. P. and Miles, R. B., "Megahertz Visualization of Compression-Corner Shock Structures," *AIAA Journal*, Vol. 39, No. 8, 2001, pp. 1542–1546.

[18]Wu, M. and Martin, M. P., "Analysis of Shock Motion in Shockwave and Turbulent Boundary Layer Interaction using Direct Numerical Simulation Data," *Journal of Fluid Mechanics*, Vol. 594, 2008, pp. 71–83.

[19]Ganapathisubramani, B., Clemens, N. T., and Dolling, D. S., "Effects of upstream boundary layer on the unsteadiness of shock-induced separation," *Journal of Fluid Mechanics*, Vol. 585, 2007, pp. 369–394.

[20]Dussauge, J. P., Dupont, P., and Debiève, J. F., "Unsteadiness in Shock Wave Boundary Layer Interactions with Separation," *Aerospace Science and Technology*, Vol. 10, No. 2, 2006.

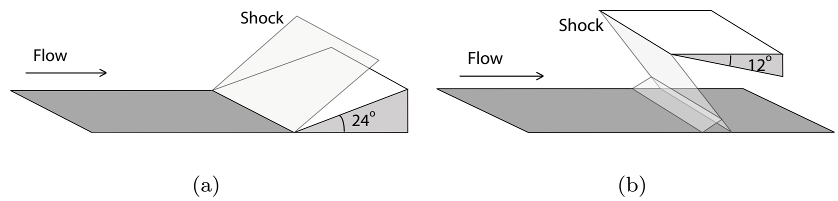

Figure 1. Canonical STBLI configurations: Inviscid flow schematic for (a) compression ramp, and (b) reflected shock configuration.

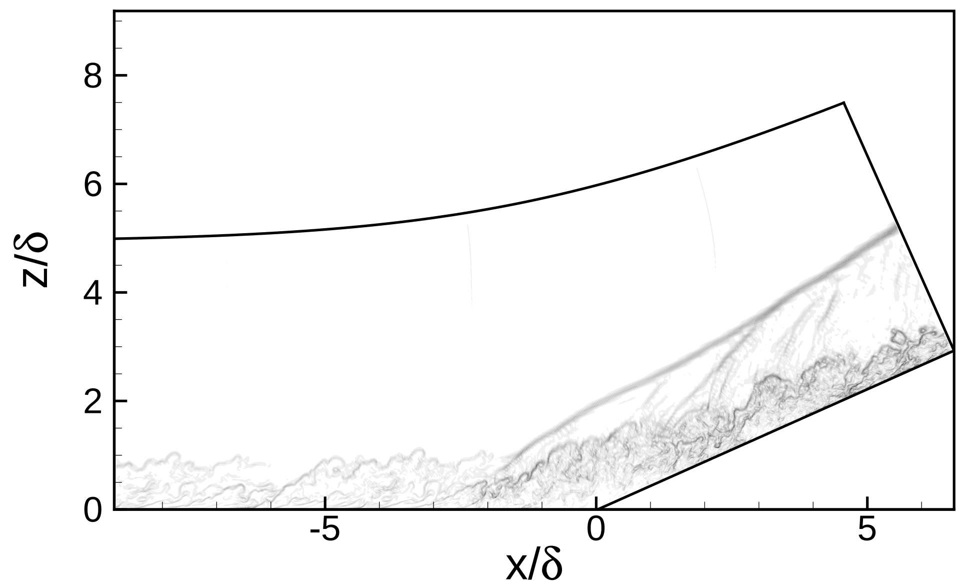

Figure 2. Instantaneous numerical schlieren visualization for the compression corner DNS.

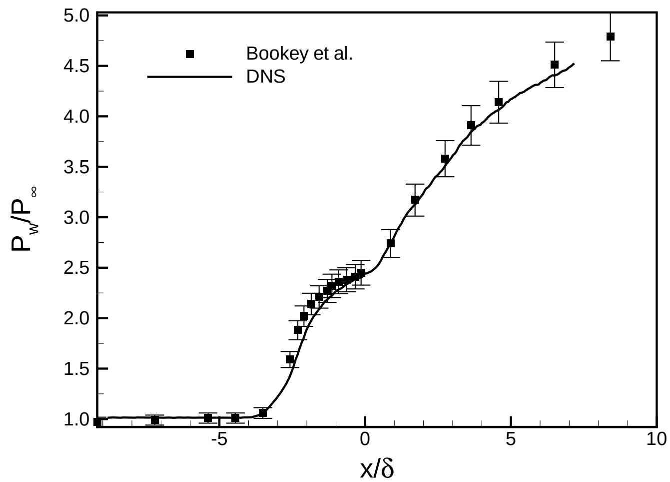

Figure 3. Mean wall-pressure vs. streamwise distance for the DNS and for the experiments of Bookey et al.[13]

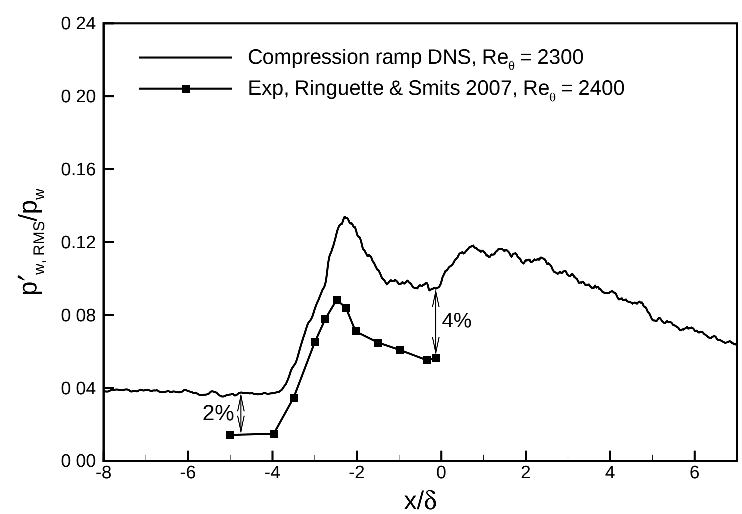

Figure 4. Fluctuating wall-pressure vs. streamwise distance for the compression ramp flow.

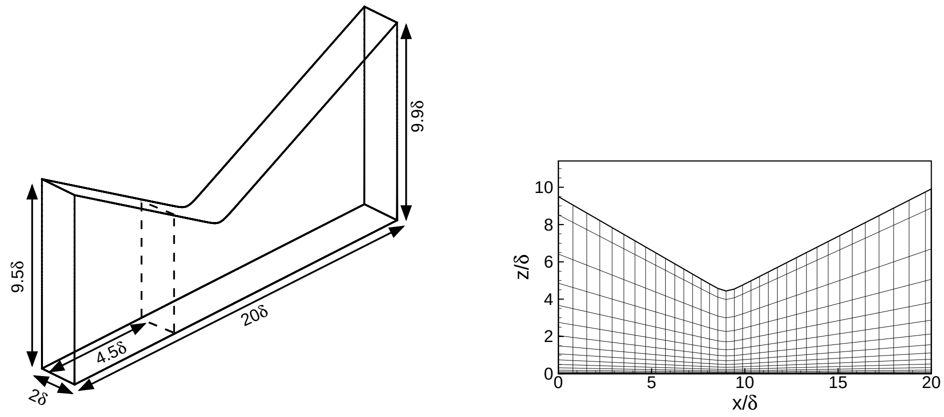

(a) (b)

Figure 5. Computational setup for the DNS of the reflected shock configuration: (a) computational domain, and (b) sample grid.

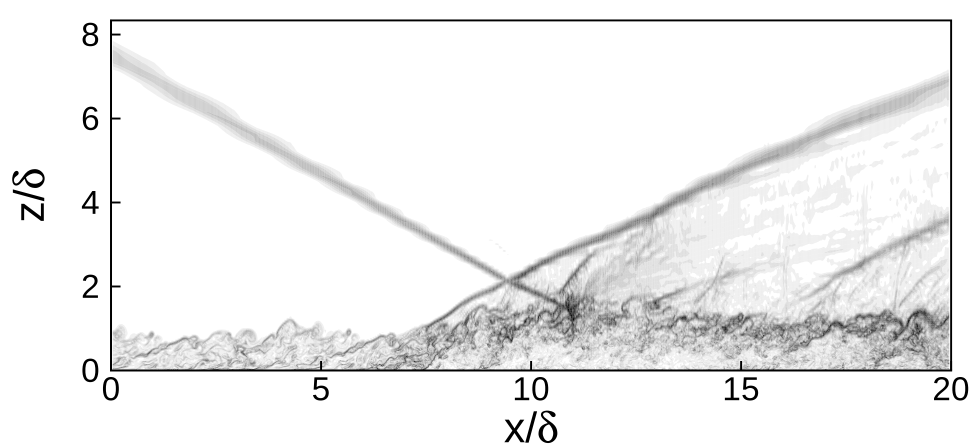

Figure 6. Instantaneous numerical schlieren visualization for the reflected shock DNS.

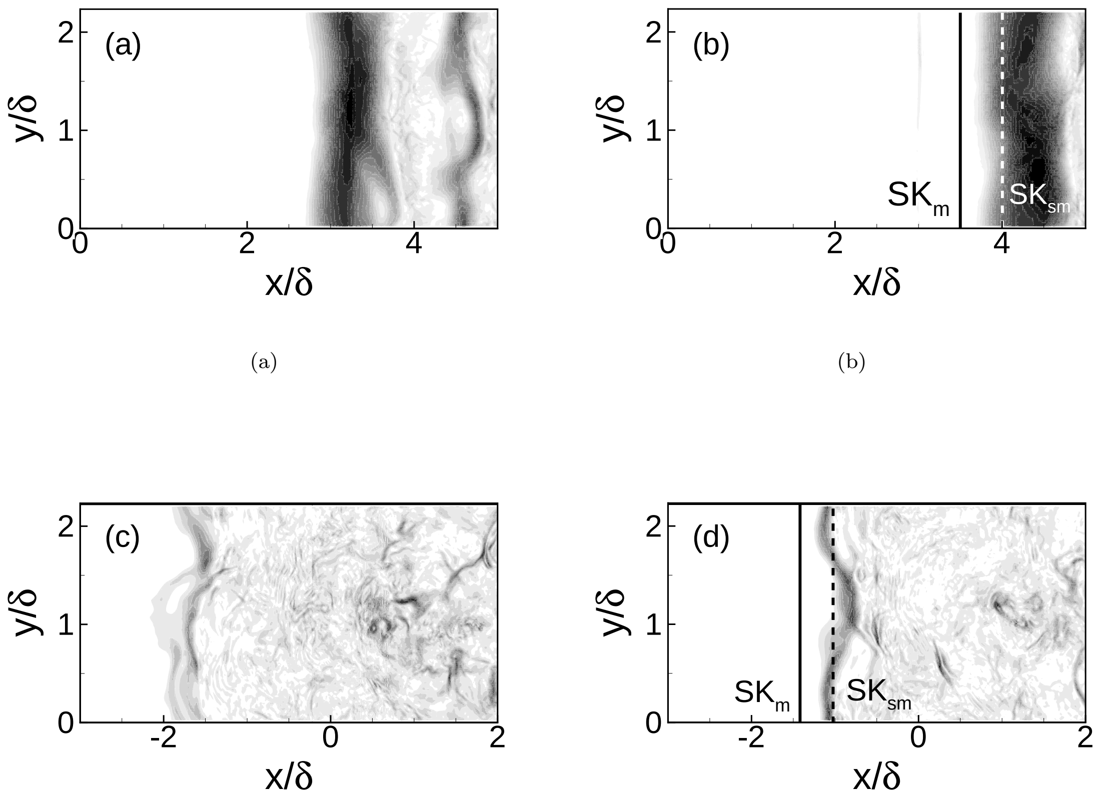

(a) (b)

(c) (d)

Figure 7. Illustration of the shock motion for the compression corner DNS. (a,b) Contours of $|\nabla p|$ in a wall-normal plane 2δ above the wall, (c,d) contours of $|\nabla p|$ in a wall-normal plane 0.9δ above the wall. The flow realization shown in (b,d) occurs $50\delta/U_\infty$ after that shown in (a,c).

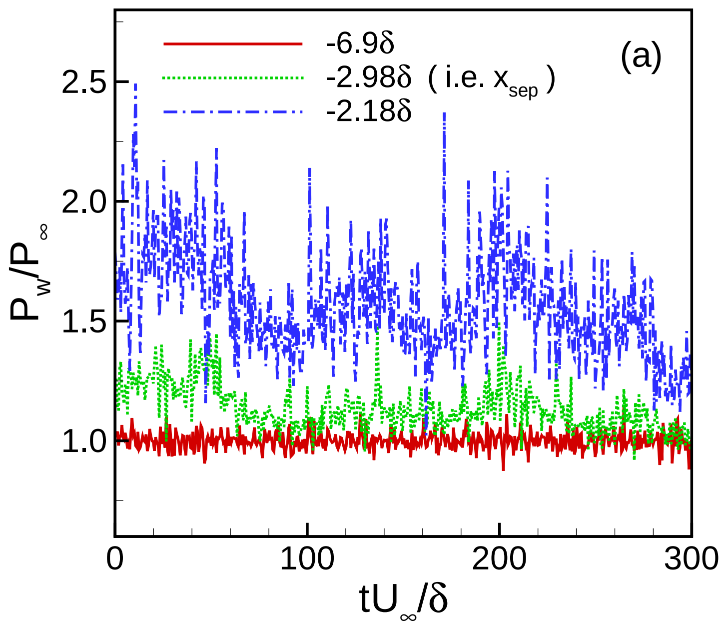

(a)

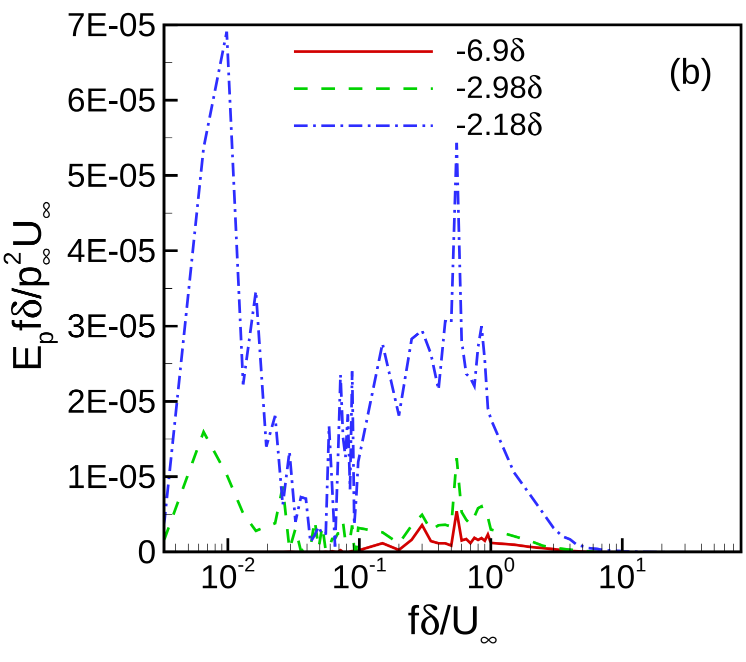

(b)

Figure 8. DNS of compression corner case: (a) Wall-pressure signals at different streamwise locations and (b) corresponding spectra.

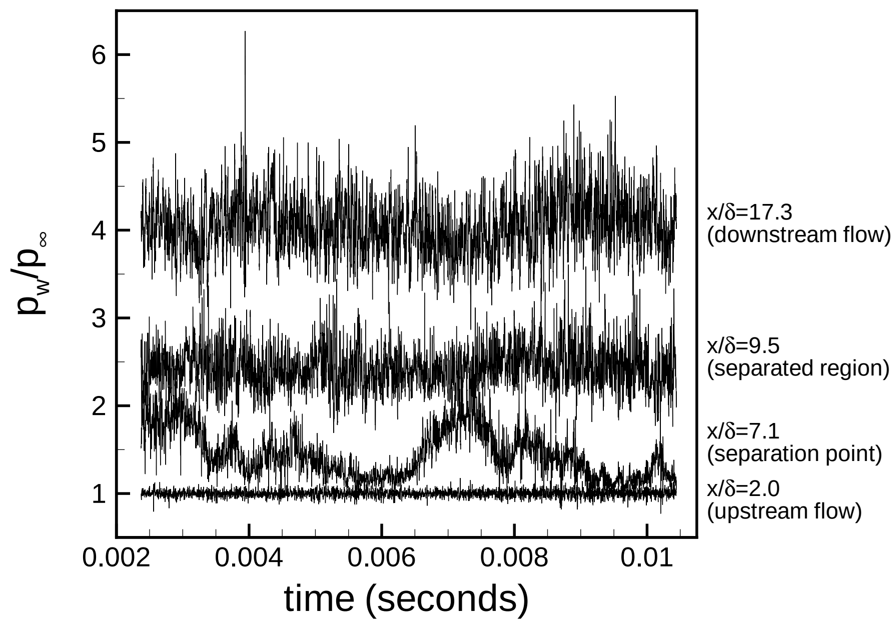

(a)

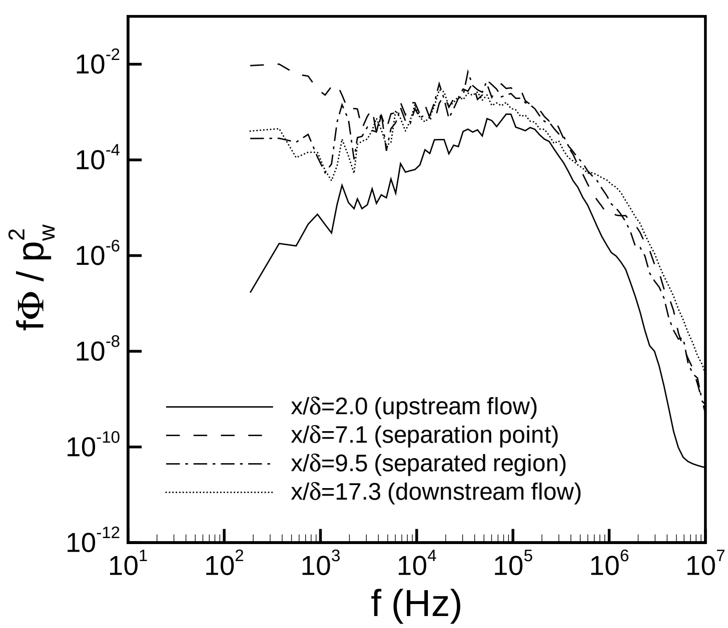

(b)

Figure 9. DNS of reflected shock case: (a) Wall-pressure signals at different streamwise locations and (b) corresponding spectra.

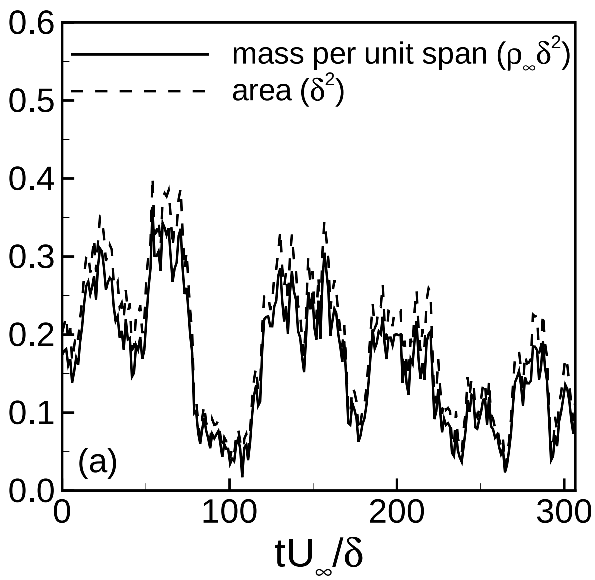

Figure 10. Mass and area of the reverse flow region.

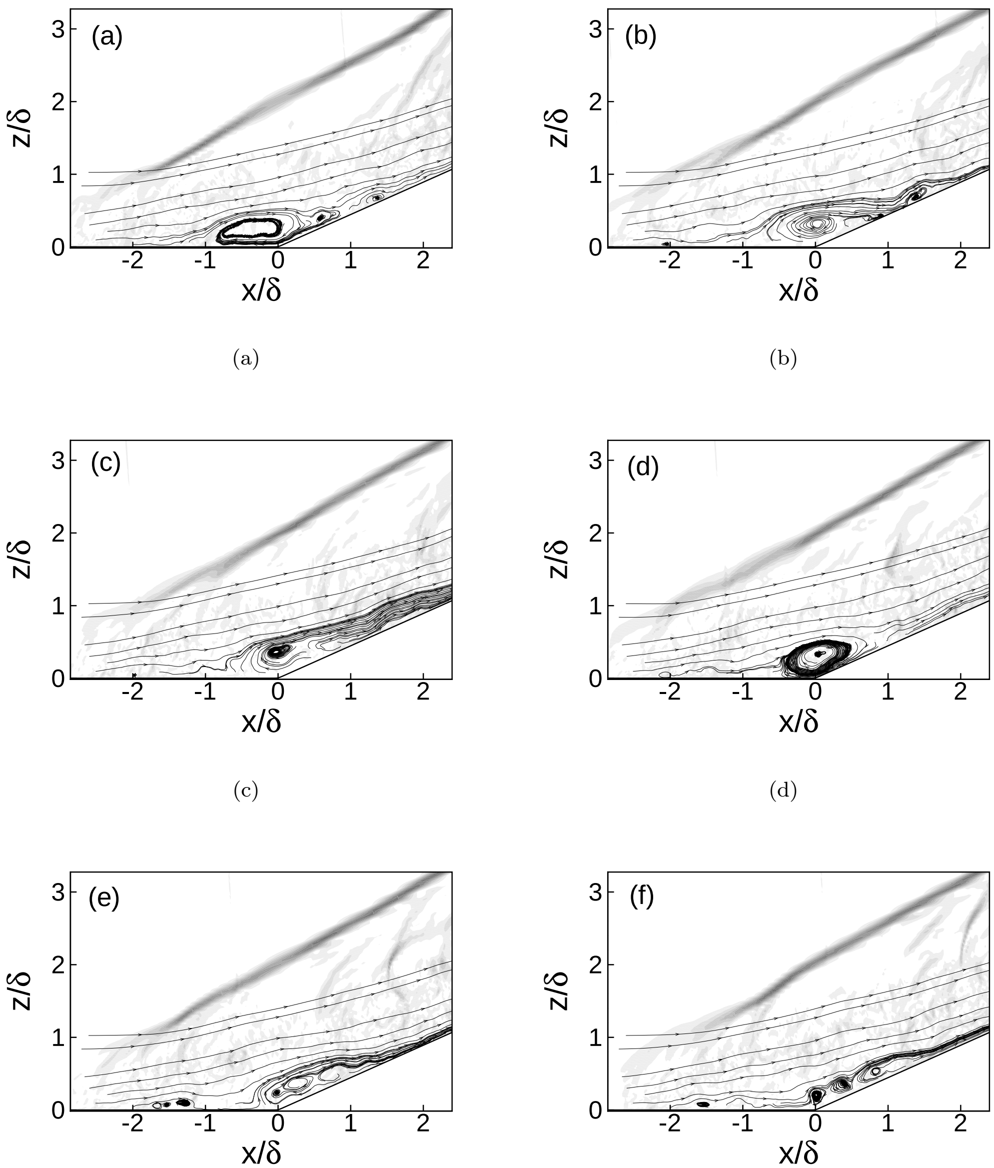

(a) (b) (c) (d) (e) (f)

Figure 11. Six instantaneous flow visualizations for the compression ramp DNS. The time interval between frames is $1\delta/U_\infty$. Streamlines and contours of gradient of pressure are shown in a streamwise-wallnormal plane.

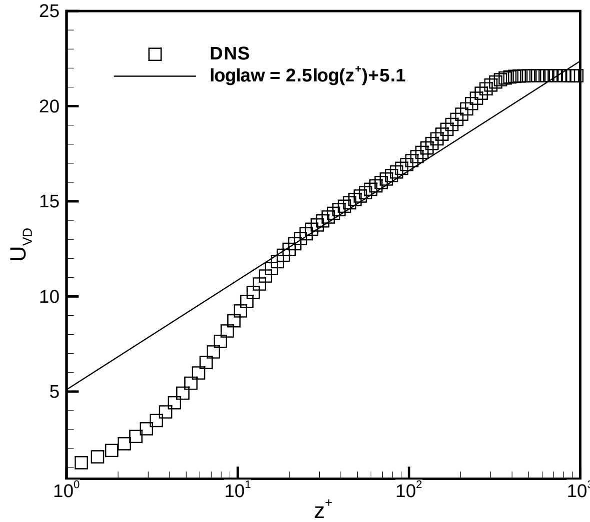

Figure 12. Van Driest-transformed velocity profile for the filtered boundary layer DNS.

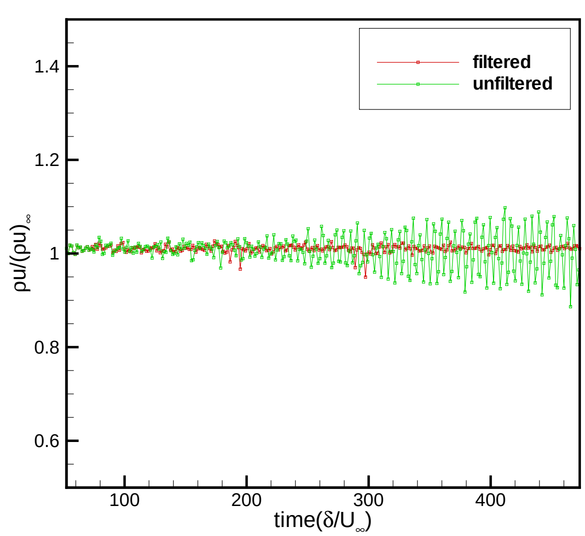

Figure 13. Spanwise-averaged mass-flux signal in the freestream (z=1.6δ).

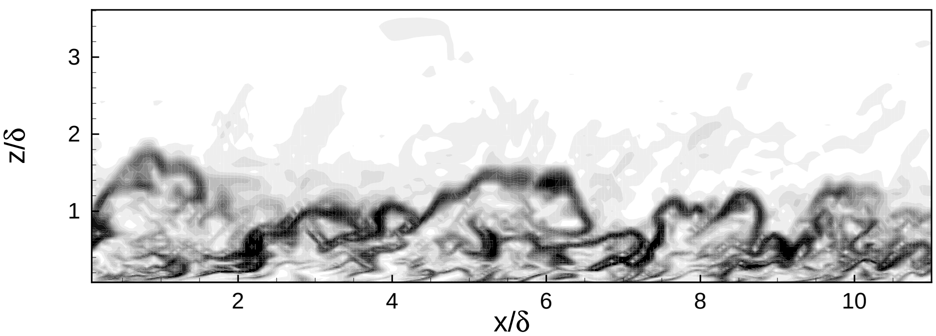

Figure 14. Instantaneous numerical schlieren visualization of the DNS of a Mach 7.8 boundary layer.